Journal of
Synchrotron Radiation
ISSN 0909-0495

Received 8 July 2005
Accepted 14 November 2005

Feedback system of a liquid-nitrogen-cooled double-crystal monochromator: design and performances

Olivier Proux,[a]* Vivian Nassif,[b] Alain Prat,[c] Olivier Ulrich,[b] Eric Lahera,[a] Xavier Biquard,[b] Jean-Jacques Menthonnex[a] and Jean-Louis Hazemann[c]

[a]Laboratoire de Géophysique Interne et Tectonophysique, UMR CNRS/Université Joseph Fourier, 1381 rue de la Piscine, Domaine Universitaire, F-38400 Saint-Martin-D'Hères, France, [b]CEA/Grenoble, DRFMC/SP2M/NRS, 17 avenue des Martyrs, F-38054 Grenoble CEDEX 9, France, and [c]Laboratoire de Cristallographie, CNRS, 25 avenue des Martyrs, BP 166, F-38042 Grenoble CEDEX 9, France. E-mail: proux@grenoble.cnrs.fr

A new set-up is reported of an indirect cryogenic cooling system for a double-crystal monochromator which runs on the BM30b/FAME beamline at the ESRF (Grenoble, France). This device has been conceived to limit the vibrations on the first diffracting crystal and to maintain it at a constant temperature. These points are crucial for maximizing the beamline stability. Moreover, the relative angular position of the second crystal can be dynamically adjusted by a piezoelectric transducer coupled with a feedback system in order to always be at the maximum of the rocking curve during an X-ray absorption spectroscopy scan. The temperature is stabilized to an accuracy of 0.01°, with two principal consequences. The energy resolution is close to the theoretical value [$\Delta E/E = 5.6 \times 10^{-6}$ for Si(220)] and the precision of the energy positioning is extremely good even if the power load changes. A feedback mechanism allows a permanent and automatic optimization of the angle between the two crystals of the monochromator. The intensity of the monochromatic beam remains optimized (i) when the intensity of the electron beam decreases in the storage ring and (ii) during an energy scan.

Keywords: double-crystal monochromator; cryogenic cooling; parallelism adjustment; X-ray absorption spectroscopy.

1. Introduction

FAME is the French absorption spectroscopy beamline for material and environmental sciences at the ESRF (France), one of the four French Collaborating Research Group (CRG) beamlines. FAME is dedicated to X-ray absorption spectroscopy (XAS). A wide range of fields such as environmental and earth sciences, electrochemistry, catalysis, biology and solid-state physics require the extraction of electronic and local structure information of very diluted elements. The stability requirements of low-concentration XAS studies and the operational simplicity of the beamline for the users were the main leading factors in the design of the whole beamline, especially the monochromator, designed and realised by our team.

The double-crystal monochromator can be schematically divided into three parts: the axis, the cooled flat first crystal and the sagitally bent second crystal. The axis was completely characterized before its installation on the beamline (Proux *et al.*, 2005). The bender of the second crystal was developed in collaboration with the ESRF optics group ten years ago and successfully used on numerous beamlines (Hazemann *et al.*, 1995). The support of this second crystal was carefully designed in order to achieve a perfect decoupling between all the second-crystal movements, and between the relative positions of the first and second crystals during Bragg-angle rotation.

During the conception and commissioning phases of the monochromator, we always kept in mind three factors which were crucial for all the optical elements: (i) the quality of the cooling devices and their thermal stability (Bilderback *et al.*, 2000), (ii) the limitations of the vibrations due to the pumping and cooling systems (Hettel, 1989) and (iii) the permanent maximization of the beamline transmittance (especially linked to the optimization of the parallelism between the two crystals). In this paper we will show how we managed to build FAME's monochromator in order to meet these requirements. We will describe the first-crystal cooling principle (§3), the second-crystal feedback adjustment (§4) and the achieved performances (§5).

doi:10.1107/S0909049505037441

2. State of the art

2.1. Monochromators cooling principles

Silicon crystal monochromators close to liquid-nitrogen (LN_2) temperatures are now commonly used at third-generation synchrotron radiation sources (Bilderback *et al.*, 2000; Bilderback, 1986), on insertion-device beamlines but also on bending-magnet beamlines. For temperatures lower than or around 120 K, the thermal expansion of silicon is close to zero and its thermal conductivity ($600\ \mathrm{W\ m^{-1}\ K^{-1}}$ at 125 K; Carpentier *et al.*, 2001) is slightly higher than that of copper at room temperature (around $450\ \mathrm{W\ m^{-1}\ K^{-1}}$). The thermal distortion of the silicon is then minimized: the lack of a thermal bump leads to an optimization of the energy resolution. The cooling process is commonly achieved by directly cooling the diffracting crystal (Knapp *et al.*, 1995; Rowen *et al.*, 2001; Dufresne *et al.*, 2002; Zhang *et al.*, 2003) or the heat exchangers which clamp this crystal (Carpentier *et al.*, 2001; Chumakov *et al.*, 2004) or that are simply in contact with it through a strain-relieving system (Comin, 1995). LN_2 cooling for the first crystal was then chosen from the beginning of the design of the beamline. With respect to water-cooled crystals, cryogenic-cooled crystals are not limited in their heat-transfer performance by the material properties (Rogers & Assoufid, 1995).

However, various parameters pointed out in the literature led us to choose a slightly different system than those commercially found. In most of the cases, LN_2 circulation is pressurized (typically between 0.2 and 1 MPa) to prevent the appearance of vapour nitrogen. The refill of the LN_2 tank can increase the pressure inside the closed-loop circulation (around 0.01 MPa) leading to a small angular displacement of the crystal (Dufresne *et al.*, 2002; Alkire *et al.*, 2000). A second factor has to be checked with care, *i.e.* the vibrations on the diffracting crystal. These vibrations may result from the circulation of LN_2 if the flow is not completely laminar and/or by the nitrogen bubbles created during the heat-exchange process. Finally, the diminution of the heating power to the first crystal, during the decay of the intensity of the electron current in the storage ring, can cause a small decrease in the temperature of the diffracting silicon volume, even if the thermal properties are optimized around 120 K.

2.2. Feedback systems for double-crystal monochromators

Various feedback systems have been detailed in the literature which maximize the output from a double-crystal X-ray monochromator or stabilize it at a given offset from its maximum to improve the harmonic rejection. These systems are suitable for stepper motors (Siddons, 1998; Jemian, 2002), piezoceramic electrostrictive actuators (Shard *et al.*, 1998) or piezoelectric transducers (PZT) (Bridges, 1987; Ramanathan *et al.*, 1988; Jemian, 2002). The optimization of the $\delta\theta$ angle between the two crystals is then achieved by maximizing either the signal proportional to the intensity of the monochromatic beam measured after the monochromator (I_0) or the intensity of the transmitted beam (or of the fluorescence current) through (or delivered by) the sample.

In the latter case (Bridges, 1987), the sample vibrates at a frequency above 10 Hz, a lock-in detection extracts the signal and dynamically controls the PZT voltage and so $\delta\theta$. This kind of adjustment is now used to maximize the intensity of the sample diffracting peaks measured during diffraction anomalous fine-structure experiments (Cross *et al.*, 1998; Renevier *et al.*, 2003). The direct optimization of the monochromator transmittance can also be achieved by maximizing the I_0 value (Shard *et al.*, 1998), the I_0 value normalized by the intensity of the electron storage ring (Ramanathan *et al.*, 1988; Siddons, 1998) or that normalized by the intensity of the white beam before the monochromator (Jemian, 2002).

3. First-crystal monochromator cooling device

The leading ideas for the monochromator cooling device are: no thermal bump, no vibration and optimal thermal stability. We decided to work in two directions in order to limit the vibrations of the first crystal brought by the LN_2 circulation. Firstly, the vibrations are damped before the crystal. Secondly, the vibrations of the LN_2 circulation are themselves limited at each point of the device. The stabilization of the first-crystal temperature is performed using a system with a large heat inertia, in order to eliminate the temperature fluctuation due to the fast evolution of the heat power on the sample (displacement of the slits during the alignment procedure, for example). Moreover, to achieve this stabilization, the first crystal can be directly heated to keep its temperature constant.

3.1. Internal cooling device

The internal first-crystal cooling device is shown in Figs. 1 and 2. The crystal is indirectly cooled at T_{crystal}. The media between the heat exchanger and the crystal serves two purposes: it has good heat-transfer capacity and vibration damping properties. The 110 mm-long heat exchanger is composed of 61 cooling fins (of diameter 3 mm) regularly spaced and carved in the copper block. The interaction surface area is maximized at around $630\ \mathrm{cm^2}$. The LN_2 flow cross section is strongly expanded, from $7\ \mathrm{mm^2}$ before the exchanger (internal diameter of the tube, 3 mm) to $4.3\ \mathrm{cm^2}$ inside it. The fluid velocity is then reduced to ensure a laminar flowing mode, limiting turbulent flow vibrations in the exchanger.

The copper braids (item 2 in Fig. 2, mean diameter $\sim$100 µm) are fixed to the silicon support piece (3) using three silicon cylindrical pieces, mechanically maintained with screws (4), the thermal contact being ensured by French alloy (Woods metal, $Bi_{50\%}Pb_{25\%}Sn_{12.5\%}Cd_{12.5\%}$, saturated with indium; 12.5 g of Woods for 8.5 g of In). The diffracting silicon crystal (1) is linked to the support piece by gallium.

The thermal bridge (12) which supports the first-crystal device is composed of three stainless steel tubes to ensure an optimal rigidity linked by an Invar ($Fe_{64\%}Ni_{36\%}$) plate (15). The choice of Invar has been made because its contraction between 300 and 80 K (0.016%) is close to the contraction of silicon, 0.023% (Marot *et al.*, 1992). Moreover, its thermal

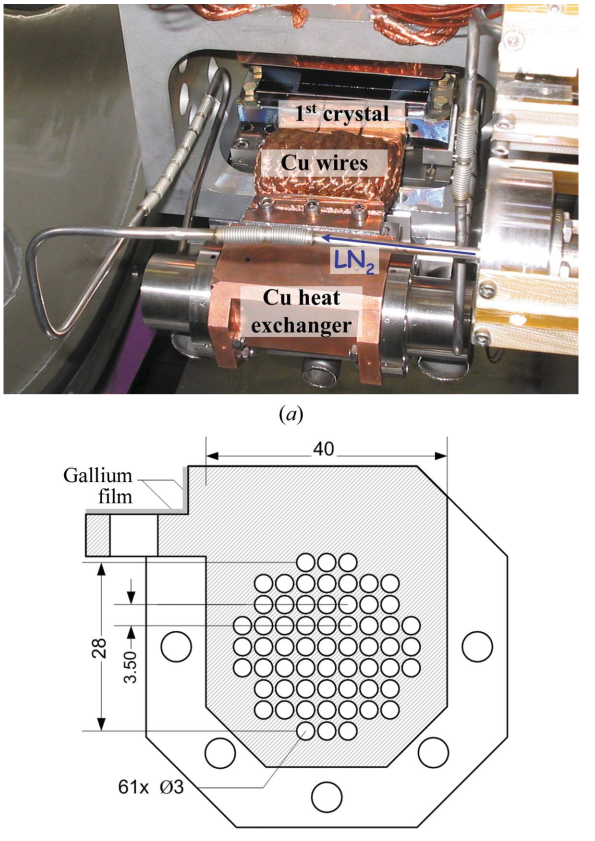

(*a*)

(*b*)

Figure 1
First-crystal cooling device fixed on the monochromator axis *via* a thermal bridge (*a*) and Cu heat-exchanger schematic detail (*b*, transversal cut).

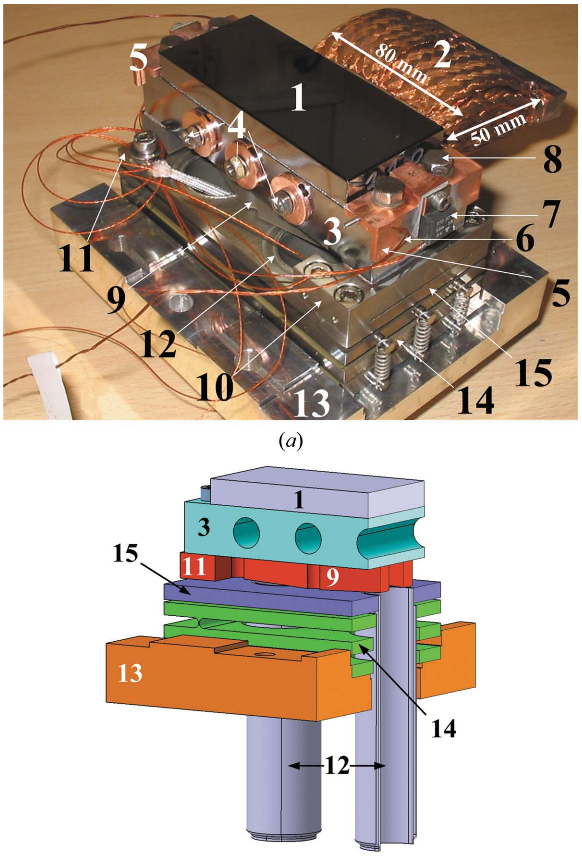

(*a*)

(*b*)

Figure 2
Photograph (*a*) and drawing (*b*) of the first-crystal complete block. 1: first Si diffracting crystal. 2: Cu braids. 3: Si support piece. 4: extremity of silicon fingers. 5: fixing Cu L-shaped part. 6: thermocouple. 7: heating resistance. 8: Invar screw. 9: weak point hinge. 10: moving stainless steel piece. 11: fixed stainless steel piece. 12: thermal bridge. 13: main holder. 14: weak points system for the manual positioning of the first-crystal surface with respect to the rotation axis. 15: Invar plate.

conductivity (around 8.5 W m^{-1} K^{-1} at 115 K) is smaller than that of silicon: the Invar plate works as a thermal screen. The fixation to the thermal bridge is indirect, ensured by a block which can accept the thermal contraction of the silicon support piece. The support is fixed with two Invar screws (8) on a stainless steel piece (10) *via* a gold foil. This moving stainless steel piece is linked to the fixed one (11) by two symmetric hinges (9). The crystal temperature can be adjusted with two symmetric heating resistances on each crystal side (7) and monitored using a K thermocouple (6) linked to a copper L-shaped part (5). The regulation of the temperature is ensured with a Eurotherm system which controls the power supply. Temperature stabilization is then achieved to an a accuracy of 0.01°.

Copper braids are strongly fixed to the 70 mm-long copper heat exchanger with three M8 screws and *via* a gallium film in order to ensure a good thermal contact (Fig. 1*b*). The effective section of the 50 mm-long braids is 6 cm^2. An estimation of the power ($\Delta Q_{\rm Cu}$) dissipated by such a copper device is given by the following relation,

$$\Delta Q_{\rm Cu} = S/l\,\left[\Lambda\left(T_{\rm silicon\,support}\right) - \Lambda\left(T_{\rm exchanger}\right)\right], \qquad (1)$$

where S and l are the effective section and the length of the copper braids, respectively, and Λ is the integrated thermal conductivity of copper. $T_{\rm silicon\ support}$ is the temperature of the Cu braids close to the first-crystal Si holder interface. $T_{\rm exchanger}$ equals the LN_2 temperature, 77 K. At equilibrium, the total dissipated power (ΔQ) equals that received, coming from both the white X-ray beam ($Q_{\rm Xray}$) and the thermal radiation owing to the monochromator's vessel and other elements having a temperature of ~300 K ($Q_{\rm radiations}$). With the cooling device not entirely being made of bulk copper, its thermal properties are slightly modified compared with those obtained theoretically from equation (1) for pure copper. Then, one can write

$$Q_{\rm Xray} = \Delta Q - Q_{\rm radiations} = \alpha\Delta Q_{\rm Cu} - Q_{\rm radiations}, \qquad (2)$$

where α is characteristic of the modification of the thermal properties of our device compared with bulk copper.

The 'crystal temperature' was measured on the silicon holder with or without the white X-ray beam. The obtained values are reported in Fig. 3, with the corresponding $Q_{\rm Xray}$ power brought by the X-ray beam and calculated using the *XOP-shadow* code (Dejus & del Rio, 1996). The experimental points were adjusted using the semi-empirical equation (2) *via* the α and $Q_{\rm radiations}$ parameters. Adjustment gives an α value equal to 0.5 and a $Q_{\rm radiations}$ value of 32 W.

Our complete set-up contributes then to a thermal conductivity degradation of 50% with respect to that of bulk copper. This decrease in the thermal properties is the consequence of the indirect cooling of the first crystal. The Cu braids, used in order to reduce the vibrations, lead to the following interfaces, which introduce thermal resistances on the path from the exchanger to the thermocouple linked to the silicon support:

(i) Cu–Cu interface between the exchanger and the braids, *via* a gallium film (Fig. 1*b*),

(ii) Cu–Si interface between the braids and the silicon fingers, *via* French alloy (elements 2 and 4 in Fig. 2),

(iii) Si–Si interface between the fingers and the support piece, *via* French alloy (element 3 in Fig. 2),

(iv) Si–Cu interface between the silicon support piece and the fixing copper part for the thermocouple, *via* an Au foil (element 5 in Fig. 2).

However, even with these reduced thermal properties, the cooling device allows one to work in the optimal temperature range for silicon. Under the usual experimental conditions, the X-ray power is in the 50–60 W range, leading to a first-crystal temperature of ∼105–110 K.

3.2. Internal LN_2 circulation

The LN_2 flow inside the monochromator is sketched in the inset of Fig. 4. The stainless steel tubes and bellows allow the rotation of the heat exchanger without strain. Two thermal bridges on the monochromator vessel stop the vibrations given by the LN_2 flow. Moreover, the use of special bellows (thickness of the wall, 15/100 mm) decreases the transmission of the vibrations.

3.3. External LN_2 circulation

The external circulation of LN_2 is purely gravitational (Fig. 4). The flow can be adjusted using two valves (5 and 6), just after the Dewar (3) and just before the monochromator (7). This allows a precise flow optimization. Moreover, in this geometry the Dewar works as a phase separator. No gaseous nitrogen is mixed in the LN_2 flux, which would strongly decrease the heat exchanger efficiency.

Even if the Dewar is at atmospheric pressure, the position of the beam after the monochromator is slightly perturbed during its refill (valve 2 opened). The control of the motorized valve (5) by a Eurotherm system allows a complete and precise management of the Dewar. The complete stage of this refill is then divided into different steps:

(i) In operation, the motorized valve is opened to ∼10% of its maximum.

(ii) When the LN_2 Dewar level reaches 30% of its total capacity (100 l), the refill procedure cycle is started (duration around 5 min, every 5 h).

(iii) Valve 5 is closed, valve 2 is opened. The LN_2 flow through the monochromator remains constant, the 4 m-long tubes between valve 5 and the monochromator entrance being then considered as a tank (capacity of the LN_2 tubes ∼0.7 l).

(iv) When the LN_2 Dewar level reaches the high level (70%), valve 2 is closed and, after 30 seconds, valve 5 is opened to 100% to eliminate the N_2 gas from the tubes.

(v) After 1 min, the aperture of valve 5 returns to its initial value.

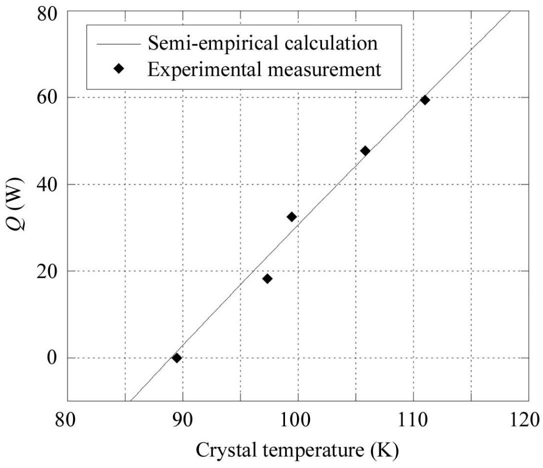

Figure 3
Evolution of the heating power owing to the incoming X-ray white beam as a function of the first-crystal temperature. Experimental points and semi-empirical values are shown.

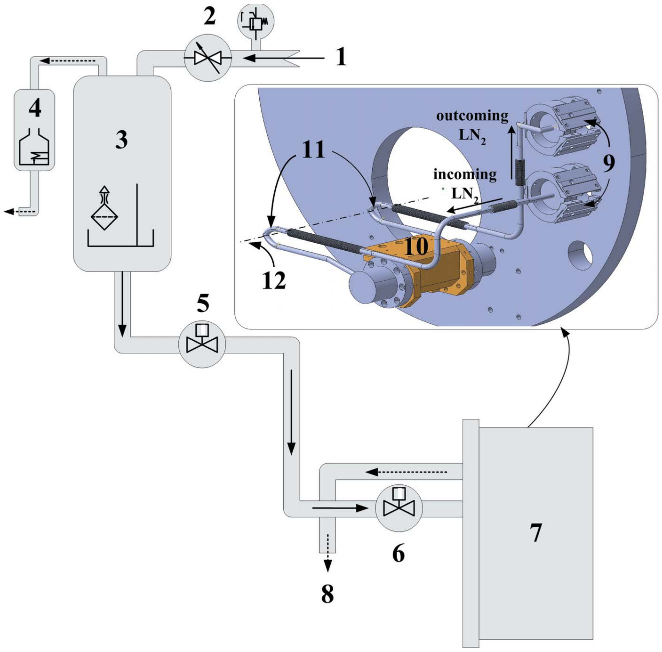

Figure 4
Scheme of the LN_2 circulation. 1: LN_2 flux from ESRF tank. 2: pneumatic valve. 3: LN_2 Dewar at atmospheric pressure. 4: heater for the N_2 cold vapour produced inside the LN_2 tank (especially during the refill of 3). 5 and 6: motorized pneumatic valves. 7: monochromator (*cf.* inset). 8: exit of the N_2 cold vapour. Continuous and dashed arrows: liquid and gaseous circulations, respectively. Internal diameter of the LN_2 tubes: 15 mm. Inset: LN_2 circulation inside the monochromator. 9: thermal bridges. 10: copper heat exchanger. 11: bellows. 12: monochromator rotation axis.

Table 1
Numerical values obtained for two crystallographic orientations.

$\delta\theta$ is the difference between the $\theta_{\rm Bragg}$ values of the first and the second crystals. $\omega_{\rm Darwin}$ is the Darwin width of the crystal. The interplanar distances are calculated from the *a* lattice parameters and the linear expansion of Si (Marot *et al.*, 1992).

	Si(111)	Si(220)
d_{hkl} (Å) at T = 125/300 K	3.13560/3.13633	1.92015/1.92059
Energy range (keV)	4–25	5–40
$\delta\theta$ range (µrad)	132.2–18.4	193.7–19.0
$\Delta\delta\theta$ range (µrad)	32.1–0.7	47.5–0.5
$\Delta\delta\theta > \omega_{\rm Darwin}/10$ (keV)	$E < 16.2$	$E \lesssim 44$

4. Closed-loop feedback to optimize the X-ray flux through the monochromator

4.1. Temperature differences considerations

The feedback mechanisms are often used to increase the stability over a long period, particularly under the decrease of the heat load on the monochromator encountered in synchrotron radiation operations. In our case, the first-crystal temperature is kept constant and the goal of the feedback device here is to counterbalance the effect of the temperature difference between the first and the second crystals, around 120 and 300 K, respectively. Their d_{hkl} parameters are different (Table 1), leading to a small difference $\delta\theta$ between the Bragg angles ($\theta_{\rm Bragg}$),

$$n\lambda = 2d_{hkl}\sin\theta_{\rm Bragg}, \qquad (3)$$

where $\lambda\,[\text{Å}] = 12.3984/E\,[\text{keV}]$ is the wavelength of the diffracted beam directly linked to its energy E, and n is the order of diffraction ($n = 1$ in this case).

Equation (3) in the differential form gives

$$\delta\theta = \tan\theta_{\rm Bragg}\delta d/d_{hkl}. \qquad (4)$$

The $\delta\theta$ value evolves during an XAS energy scan, the evolution being larger for Si(220) than for Si(111). This $\delta\theta$ evolution is quantified for a typical 1 keV energy EXAFS scan,

$$\Delta\delta\theta(E) = \delta\theta_E - \delta\theta_{E+1}. \qquad (5)$$

The obtained $\Delta\delta\theta(E)$ curves are shown in Fig. 5.

4.1.1. Consequence on the X-ray beam intensity. The $\Delta\delta\theta(E)$ absolute difference values are significant, especially by comparison with the Darwin width of the crystals, $\omega_{\rm Darwin}$, their theoretical angular acceptance given by the following equation,

$$\omega_{\rm Darwin} = \left[2r_{\rm e}\lambda^2 C|F(hkl)|\exp(-M)\right]/\left[V\pi\sin\left(2\theta_{\rm Bragg}\right)\right], \qquad (6)$$

where $r_{\rm e}$ is the classical electron radius, C is the polarization factor (equal to 1 in this case), $F(hkl)$ is the structure factor and $\exp(-M)$ is the Debye–Waller factor (= 1). The $\omega_{\rm Darwin}/10$ curves are shown in Fig. 5 for the two crystallographic orientations (111) and (220), assuming that a $\Delta\delta\theta$ evolution larger than $\omega_{\rm Darwin}/10$ needs a $\delta\theta$ feedback during an EXAFS scan.

For the Fe K-edge (7.112 keV), $\Delta\delta\theta$ equals 8.8 µrad [Si(111)] and 17.4 µrad [Si(220)], the values of the Darwin width being 39.6 µrad and 26.1 µrad, respectively. Without any $\delta\theta$ adjustment, the beam flux, optimized at the beginning of the scan, would strongly decrease, especially when using Si(220) crystals. A $\delta\theta$ feedback is then necessary in our case over the entire energy range to optimize the X-ray flux [except for energies higher than 16.2 keV when using Si(111) crystals].

4.1.2. Consequence of the vertical X-ray beam position. Another consequence of the temperature difference is the angular change of the monochromatic beam during an energy scan. A $\Delta\delta\theta(E)$ angular difference between the two crystals on a 1 keV energy scan leads to an angular evolution of the outgoing beam equal to $2\Delta\delta\theta(E)$. With the distance between the monochromator and the sample being L = 12.51 m (Proux *et al.*, 2005), the X-ray vertical position shift on the sample equals $2L\Delta\delta\theta(E)$. For the low-energy scans, these beam translations become really large compared with the vertical beam size (in the 100–200 µm range, depending on the second-mirror curvature). For the Fe K-edge, the vertical translations during the scans are 220 µm and 435 µm using Si(111) and Si(220), respectively. This motion is clearly not desirable for the study of inhomogeneous or small samples. To avoid this effect, we choose to move the experimental table during the energy scan with an accuracy of 1 µm. The position of the beam is then kept constant over the entire energy scan range with respect to the sample and all the detectors (for the transmission and fluorescence measurements), both in classical step-by-step and quick continuous EXAFS scan configurations.

4.2. Technical considerations

The implantation of the PZT in the monochromator is shown in Fig. 6. Both a micro-motor and a PZT are used. The stepper micro-motor allows coarse adjustments of the parallelism between the two crystals during the alignment procedures and for the large $\Delta\delta\theta$ evolutions. The PZT allows fine adjustments and feedback optimization *via* the lock-in system. The main interest in the PZT with respect to the micro-motor is in its positioning resolution (sub-nanometric), but also the lack of a mechanical backlash and the possibility of providing a modulated excitation.

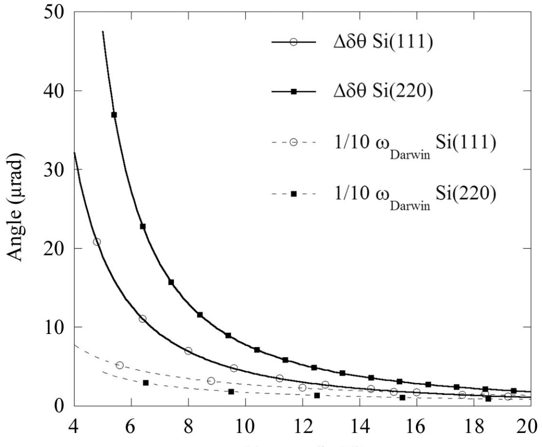

Figure 5
$\Delta\delta\theta$ and $\omega_{\rm Darwin}$ evolution with respect to energy for two crystallographic orientations.

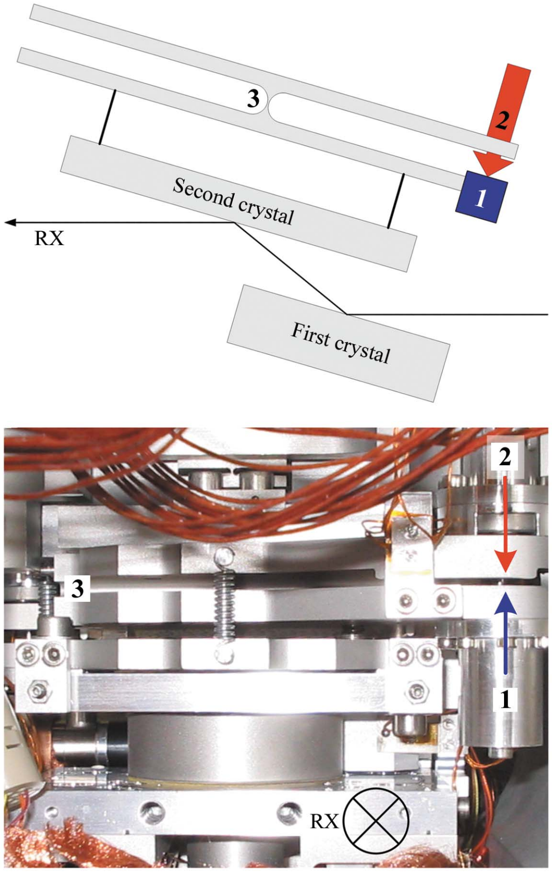

Figure 6
Sketch and photograph of the PZT implantation in the double-crystal monochromator. 1: piezoelectric transducer. 2: stepper micro-motor. 3: hinge.

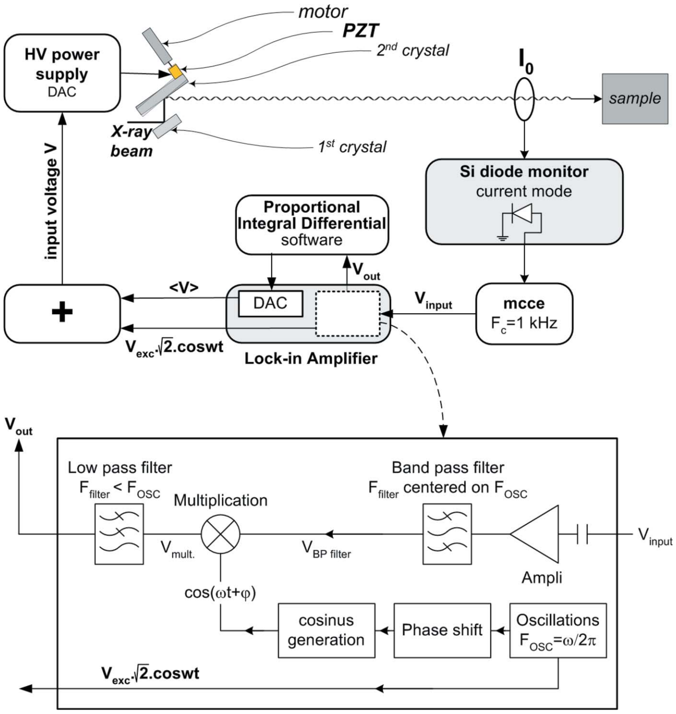

Figure 7
Block diagrams of the control system and the lock-in amplifier.

4.3. Electronic considerations

Our aim was to use only one flux measurement system (I_0, Fig. 7) as an input parameter for the feedback system, in order to decorrelate as much as possible the $\delta\theta$ adjustment from the other parameters. The system described by Shard *et al.* (1998) could not be adapted on our beamline owing to the dead-time induced by the process (minimum 1 second per point) and the impossibility of adapting it for a continuous energy scan (as used during quick-EXAFS experiments). We adapted then the system developed by Renevier *et al.* (2003) for DAFS experiments.

The idea was to measure a quantity proportional to the derivative of the rocking-curve peak. At the low- and high-angle sides of the peak maximum, the sign of the derivative is changing, whereas the derivative equals zero at the maximum. Fig. 7 shows a scheme of the set-up used.

The intensity of the transmitted beam *versus* the angular difference between first and second crystals ($\delta\theta$) can be defined as $I_0 = f(\delta\theta) = f(V)$, where V is the [0–10 V] input voltage of the PZT high-voltage supply. The V voltage, and so the $\delta\theta$ angle, is modulated with a frequency $F_{\rm OSC} = \omega/2\pi$ and an amplitude $V_{\rm exc}$ by the lock-in amplifier (EG&G instruments, 7220 DSP),

$$V = \langle V\rangle + V_{\rm exc}\,2^{1/2}\cos(\omega t) = \langle V\rangle + \Delta V_{\rm exc}. \tag{7}$$

For small $\Delta V_{\rm exc}$ modulations, a Taylor expansion of $f(V)$ to the first order is expressed by

$$f(V) \simeq f(\langle V\rangle) + \Delta V_{\rm exc}[f'(V)]_{\langle V\rangle}. \tag{8}$$

The transmitted signal $I_0 = f(V)$ is fed into the lock-in input. A block diagram of the internal process of the lock-in amplifier is sketched in the lower part of Fig. 7. The $V_{\rm mult}$ voltage is expressed as

$$V_{\rm mult} = f(V)\cos(\omega t + \varphi), \tag{9}$$

$$\begin{aligned} V_{\rm mult} \simeq{}& f(\langle V\rangle)\cos(\omega t + \varphi) \\ &+ \tfrac{1}{2}V_{\rm exc}\,2^{1/2}\,[f'(V)]_{\langle V\rangle}[\cos(2\omega t + \varphi) + \cos(\varphi)]. \end{aligned} \tag{10}$$

After the low-pass filter, the output voltage is expressed as

$$V_{\rm out} = \tfrac{1}{2}V_{\rm exc}\,2^{1/2}\,[f'(V)]_{\langle V\rangle}\cos(\varphi). \tag{11}$$

By varying the V voltage, the derivative of the rocking curve $f'(V)$ can be calculated and minimized with a simple PID (proportional-integral-derivative) software. This single PID software takes the output filter voltage $V_{\rm out}$ as an input signal. It computes a voltage command and is able to adjust this voltage $\langle V\rangle$ to maintain the θ angle at the maximum of the rocking curve.

The main interest in nulling a parameter is that in the case, for example, of electron beam loss in the storage ring or X-ray shutter closing, $I_0 = f(V)$ is constant (equal to 0) so $f'(V) = 0$ for all V values. The PZT voltage then remains constant. When the electron beam is restored, the $\delta\theta$ angle is very close to the optimal value and the optimization process is achieved very quickly.

4.4. Characteristics of the modulation

The optimal parameters are a modulation frequency $F_{\rm OSC}$ equal to 440 Hz and a modulation amplitude equal to 1 mV (high-energy experiment, $E > 20$ keV) or 2 mV r.m.s. ($E < 20$ keV). The used PZT is controlled on a 0–10 V range and its maximal elongation is 10 µm. Such a voltage modulation amplitude gives rise to an angular modulation equal to 0.015 or 0.03 µrad, much smaller than the Darwin width of the crystals [in our case, the smallest value is obtained for E = 40 keV using Si(220) crystals, $\omega_{\rm Darwin}$ = 2.76 µrad]. This modulation does not induce any noise on the monochromatic X-ray beam intensity. Moreover, the vertical displacement of the beam associated with this modulation on the sample, located at 15 m after the monochromator, is less than 0.5 µm, the minimum vertical size being around 100 µm.

5. Beamline performances

5.1. Thermal stability

The first-crystal temperature stabilization is achieved with a 0.01° accuracy at a value ranging from 103 K to 118 K. This temperature value depends on the white-beam total power on the first crystal. For example, the stabilization temperature was 103 K at the Ti *K*-edge (*K*-edge energy $E_{\rm edge}$ = 4.966 keV), 110 K at the Cu *K*-edge ($E_{\rm edge}$ = 8.979 keV) and between 114 and 116 K for the experiments performed at higher energy ($E_{\rm edge}$ > 22 keV).

The stability of the energy resolution of the beamline is directly linked to the thermal stability of the first crystal. Two sets of experiments have been performed at the Ti *K*-edge on two amorphous alloys using Si(220) crystals for the monochromator ($\theta_{\rm Bragg}$ = 40.553°). The energy reproducibility for each set of ten spectra (defined unambiguously as the first zero of the derivative curve) is ±0.03 eV.

5.2. Energy resolution

The energy resolution of the beamline can be evaluated by the different XANES features of reference compounds. Fig. 8 represents several XANES spectra obtained in the transmission mode for pure metallic references (Ti, V, Cu, Zr and Nb) at their *K*-edge. Measurements were performed using Si(220) crystals and with the maximum vertical divergences delivered by the bending-magnet source on the first mirror ($\delta\theta_{\rm diverg}$ ranges from 0.23 mrad for Ti to 0.12 mrad for Nb, depending on the 1.15 m-long first-mirror angle). The pre-edge parts of the edges are shown in the inset. These features, which are often called pre-edge fine structures, have been shown to be caused by transitions of the 1*s* electron to the unoccupied electron states near the conduction band. Such transitions are dipole-forbidden for the free atoms but can become dipole-allowed for the atoms in the matrix, because of *d*–*p* mixing. To extract these features, the contribution of the edge jump to the pre-edge was modeled by interpolating the background with a spline function, using the data several eV before and after the pre-edge. Experimental FWHM values ($\Delta E_{\rm meas}$) have then been quantified (Table 2).

Table 2

Comparison between the experimental and theoretical FWHM peak of the XANES pre-edge for metallic references, $\Delta E_{\rm electr}$, $\Delta E_{\rm diverg}$ and $\Delta E_{\rm meas}$ (eV).

E_K: *K*-edge energy (keV). $\Gamma_{\rm i}$ and $\Gamma_{\rm f}$: core–hole lifetime broadenings of the initial and final states (eV) (Fuggle & Inglesfield, 1992). $\delta\varepsilon_{\rm crystals}$: intrinsic resolution of the Si(220) crystals (eV). Transitions: 1*s* to 4*p*, in the $3d^2$ (*a*), $3d^3$ (*b*) and $3d^{10}$ (*c*) configurations (Raj *et al.*, 2002; Bazin & Rehr, 2003; Wang *et al.*, 2002; Ruckman *et al.*, 1998).

	E_K	$\Gamma_{\rm i}$	$\Gamma_{\rm f}$	$\delta\varepsilon_{\rm crystals}$	$\Delta E_{\rm electr}$	$\Delta E_{\rm diverg}$	$\Delta E_{\rm meas}$
Ti	4.966	0.94	0.1 (*a*)	0.25	0.98	5.28	1.85
V	5.465	1.01	0.2 (*b*)	0.28	1.07	6.16	1.5
Cu	8.979	1.55	1.6 (*c*)	0.46	2.27	10.6	3.4
Zr	17.998	3.84	0.09	0.92	3.95	13.4	4
Nb	18.986	4.14	0.11	0.97	4.25	14.1	4.5

The broadening of these peaks can be theoretically evaluated roughly from the core–hole lifetime broadenings of the initial and final states ($\Gamma_{\rm i}$ and $\Gamma_{\rm f}$) and from the intrinsic energy resolution of the monochromator ($\delta\varepsilon_{\rm crystals}$). $\delta\varepsilon_{\rm crystals}$ values are directly calculated for each edge energy using the $\omega_{\rm Darwin}$ values obtained for Si(220) crystals (equation 6),

$$\delta\varepsilon_{\rm crystals}/E_{\rm edge} = \delta\theta/\theta = \omega_{\rm Darwin}/\theta_{\rm Bragg}. \tag{12}$$

Assuming a Gaussian contribution of all these parameters, the total broadening owing to these electronic considerations can then be estimated *via* the following equation,

$$\Delta E_{\rm electr} = \left(\Gamma_{\rm i}^2 + \Gamma_{\rm f}^2 + \delta\varepsilon_{\rm crystals}^2\right)^{1/2}. \tag{13}$$

The efficiency of the vertical collimation of the beam by the first mirror can also be evaluated (Klementev, 2001). The vertical divergence of the incident beam, $\delta\theta_{\rm diverg}$, is larger (from 5× to 14×) than the angular acceptance of the crystals, $\omega_{\rm Darwin}$ (equation 6, Fig. 5). Without the first mirror, the energy resolution would be

$$\Delta E_{\rm diverg} = \delta\theta_{\rm diverg} E_{\rm edge} \cot\!\mathrm{an}\left(\theta_{\rm Bragg}\right). \tag{14}$$

The theoretically calculated and experimentally measured data are collected in Table 2. The $\Delta E_{\rm diverg}$ values are always larger than $\Delta E_{\rm meas}$. The vertical collimation of the beam is correctly achieved by the first mirror: the vertical divergence of the beam on the first crystal is strongly reduced with respect to the total divergence. At the reverse, the differences between the $\Delta E_{\rm meas}$ and $\Delta E_{\rm electr}$ values are small, between 0.05 eV (Zr case) and 1.13 eV (Cu case). The experimental resolution of the beamline is close to the theoretical resolution.

5.3. Optimization and stability of the beamline

The feedback system allows a dynamical optimization of the I_0 intensity during an energy scan. It leads to a significant improvement in the signal-to-noise ratio. Moreover, the device is dead-time free and therefore suitable for classical step-by-step and continuous EXAFS scans (Fig. 9).

The intensity of the X-ray monochromatic beam I_0, measured after the monochromator, decreases of course when the intensity of the current in the storage ring $I_{\rm SR}$ decreases, but the ratio I_0/I_{SR} is constant even during a storage-ring refill (*i.e.* during a strong variation in the heat power on the first crystal). The standard deviation of this ratio over a long period is then a good way to quantify the beamline stability.

Over a short period and without any energy displacement, the optimization of the beamline is achieved with a noise of ~0.03% r.m.s. for a counting time equal to 1 second per point (Fig. 10). To estimate the quality of the beamline stability over a longer period, we report in Table 3 different measurements performed during continuous experiments at various energies and various storage-ring filling modes. During these sets of experiments, no beamline optimization was performed except for the feedback adjustment. The spectra are energy scans on a 1 keV range for a total acquisition time of approximately 30–

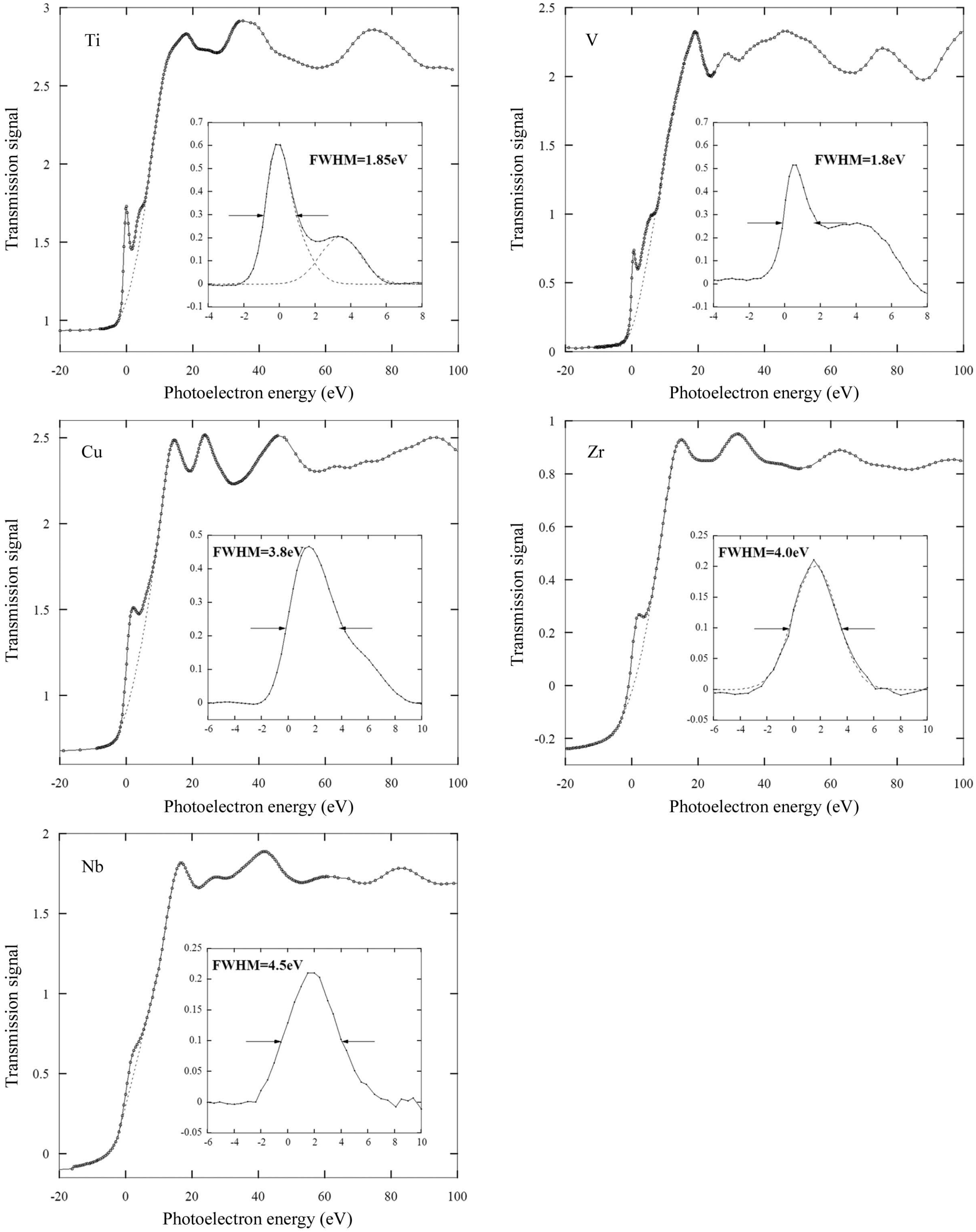

Figure 8
K-edge XANES spectra measured in transmission mode for Ti, V, Cu, Zr and Nb metallic references. Insets: edge features after edge subtraction. Crystals: Si(220).

Table 3
Measured standard deviation of the intensity of the monochromatic beam I_0 normalized by the current of the electron beam in the storage ring, I_{SR}.

Storage-ring mode: 16 bunches – lifetime 9 h, $50 < I$ (mA) < 90, one refill every 6 h; uniform – lifetime 75 h, $160 < I$ (mA) < 200, one refill every 12 h.

	Fe *K*-edge	Br *K*-edge	Zn *K*-edge	Sb *K*-edge
Energy (keV)	7.112	13.474	9.659	30.491
Storage-ring mode	16 bunchs	16 bunchs	Uniform	Uniform
Number of spectra	88 (including 3 refills)	69 (including 2 refills)	90 (including 7 refills)	54 (including 4 refills)
Standard deviation	0.6%	0.9%	2.6%	2.1%

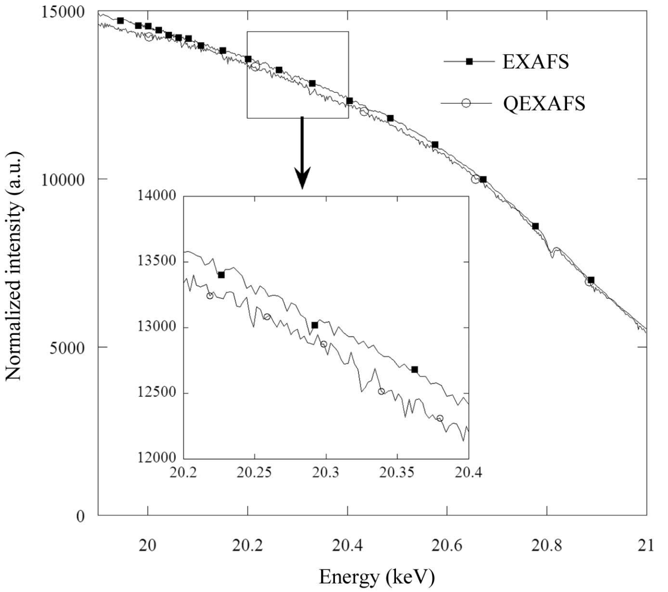

Figure 9
Monochromatic X-ray beam intensity, $I_0(E)$, normalized with the storage-ring current, $I_{SR,mA}(E)$, and with the integration time, for two kinds of acquisition modes: step-by-step (EXAFS) and continuous (QEXAFS) scans, Mo *K*-edge.

45 min. For a period of 1 day (including two or three refills), the standard deviation is lower than 1%. It increases to around 2–3% for longer periods (2 and 4 days).

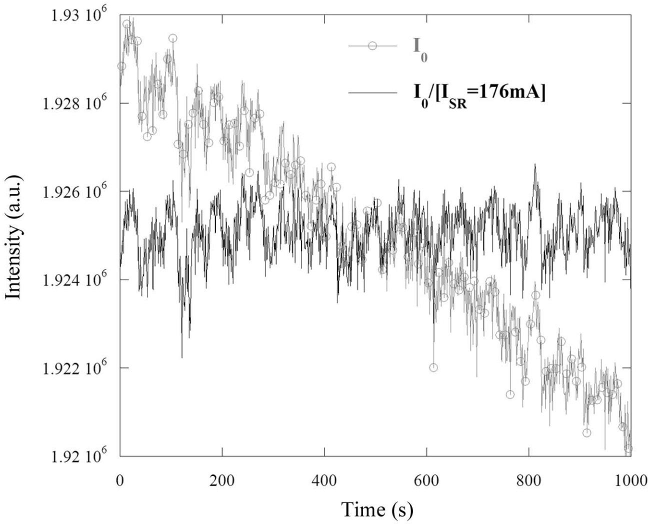

Figure 10
Monochromatic X-ray beam intensity, $I_0(t)$, as measured and normalized for a constant storage-ring current, I_{SR} = 176 mA. During the 1000 s acquisition time, I_{SR} decreased from 176.37 to 175.54 mA. Measurement 1 second per point at the As *K*-edge using Si(220) crystals (θ_{Bragg} = 15.79°).

6. Conclusion

We have investigated the design and the performances of an indirect cryogenic cooling system for a double-crystal monochromator including a second-crystal angular optimization system. The first-crystal cooling system was adjusted to avoid vibrations and to work at a constant temperature in the 95–115 K range. The automatic angular correction of the angle between the two crystals leads to an optimization of the monochromatic beam intensity, during an energy scan (in the step-by-step or continuous mode) and when the storage-ring current decreases. The performance of the monochromator (thermal stability, energy resolution and optimization over short and long periods) has been checked with care.

The stability of the electron beam position in the ESRF storage ring is extremely good. However, owing to the large distances of the optic elements and the sample with respect to the source (Proux *et al.*, 2005), even a small perturbation of the electron beam position can induce a loss in the X-ray beam stability. This stability will be improved in the near future with the dynamic control of the evolution of the position of the incident beam owing to the long-range evolution of the position of the electron beam in the storage ring (Fischetti *et al.*, 2002).

The authors wish to acknowledge the help of the ESRF technical staff and support groups, and in particular J. P. Vassalli and P. Villermet for the monochromator crystals realisation and H. P. Van Der Kleij for monochromator axis metrology. Thanks is also given to all the users who helped us in the beamline commissioning.

References

Alkire, R. W., Rosenbaum, G. & Evans, G. (2000). *J. Synchrotron Rad.* **7**, 61–68.
Bazin, D. & Rehr, J. J. (2003). *J. Phys. Chem. B*, **107**, 12398–12402.
Bilderback, D. H. (1986). *Nucl. Instrum. Methods A*, **246**, 434–436.
Bilderback, D. H., Freund, A. K., Knapp, G. S. & Mills, D. M. (2000). *J. Synchrotron Rad.* **7**, 53–60.
Bridges, F. (1987). *Nucl. Instrum. Methods A*, **257**, 447–450.
Carpentier, P., Rossat, M., Charrault, P., Joly, J., Pirocchi, M., Ferrer, J. L., Kaïkati, O. & Roth, M. (2001). *Nucl. Instrum. Methods A*, **456**, 163–176.

Chumakov, A., Rüffer, R., Leupold, O., Celse, J. P., Martel, K., Rossat, M. & Wah-Keat, L. (2004). *J. Synchrotron Rad.* **11**, 132–141.

Comin, F. (1995). *Rev. Sci. Instrum.* **66**, 2082–2084.

Cross, J. O., Elam, W. T., Harris, V. G., Kirkland, J.-P., Bouldin, C. E. & Sorensen, L. B. (1998). *J. Synchrotron Rad.* **5**, 911–913.

Dejus, R. J. & del Rio, M. S. (1996). *Rev. Sci. Instrum.* **67**, 3356.

Dufresne, E. M., Arms, D. A., Dierker, S. B., Clarke, R., Yacoby, Y., Pitney, J., MacHarrie, B. & Pindak, R. (2002). *Rev. Sci. Instrum.* **73**, 1511–1513.

Fischetti, R. F., Heurich, R., Perry, D., Stepanov, S., Kondrashkina, E. & Rosenbaum, G. (2002). *Rev. Sci. Instrum.* **73**, 1518.

Fuggle, J. C. & Inglesfield, J. E. (1992). Editors. *Topics in Applied Physics*, Vol. 69, pp. 339–350. Berlin: Springer-Verlag.

Hazemann, J. L., Nayouf, K. & de Bergevin, F. (1995). *Nucl. Instrum. Methods B*, **97**, 547–550.

Hettel, R. (1989). *Rev. Sci. Instrum.* **60**, 1501–1506.

Jemian, P. R. (2002). *Rev. Sci. Instrum.* **73**, 1533.

Klementev, K. V. (2001). *J. Phys. D*, **34**, 2241–2247.

Knapp, G. S., Rogers, C. S., Beno, M. A., Wiley, C. L., Jennings, G. & Cowan, P. L. (1995). *Rev. Sci. Instrum.* **66**, 2138–2140.

Marot, G., Rossat, M., Freund, A., Joksch, S., Kawata, H., Zhang, L., Ziegler, E., Berman, L., Chapman, D., Hastings, J. B. & Iarocci, M. (1992). *Rev. Sci. Instrum.* **63**, 477–480.

Proux, O., Biquard, X., Lahera, E., Menthonnex, J.-J., Prat, A., Ulrich, O., Soldo, Y., Trévisson, P., Kapoujyan, G., Perroux, G., Taunier, P., Grand, D., Jeantet, P., Deleglize, M., Roux, J.-P. & Hazemann, J.-L. (2005). *Phys. Scr.* **115**, 970–973.

Raj, S., Padhi, H. C., Palit, P., Basa, D. K., Polasik, M. & Pawłowski, F. (2002). *Phys. Rev. B*, **65**, 193105.

Ramanathan, M., Engbretson, M. & Montano, P. A. (1988). *Nucl. Instrum. Methods A*, **266**, 471–474.

Renevier, H., Grenier, S., Arnaud, S., Berar, J.-F., Caillot, B., Hodeau, J.-L., Letoublon, A., Proietti, M. G. & Ravel, B. (2003). *J. Synchrotron Rad.* **10**, 435–444.

Rogers, C. S. & Assoufid, L. (1995). *Rev. Sci. Instrum.* **66**, 2200–2202.

Rowen, M., Peck, J. W. & Rabedeau, T. (2001). *Nucl. Instrum. Methods A*, **467–468**, 400–403.

Ruckman, M. W., Reisfeld, G., Jisrawi Najeh, M., Weinert, M., Strongin, M., Wiesmann, H., Croft, M., Sahiner, A., Sills, D. & Ansari, P. (1998). *Phys. Rev. B*, **57**, 3881–3886.

Shard, A. G., Dhanak, V. R. & Smith, A. D. (1998). *J. Synchrotron Rad.* **5**, 829–831.

Siddons, D. P. (1998). *J. Synchrotron Rad.* **5**, 685–686.

Wang, C. M., Slade Cargill, G., Chan, H. M. & Harmer, M. P. (2002). *J. Am. Ceram. Soc.* **85**, 2492–2498.

Zhang, L., Lee, W. K., Wulff, M. & Eybert, L. (2003). *J. Synchrotron Rad.* **10**, 313–319.